

Study of image reconstruction using dynamic grids in tomographic gamma scanning

LIU Cheng GU Weiguo* QIAN Nan WANG Dezhong

School of Mechanical Engineering, Shanghai Jiao Tong University, Shanghai 200240, China

Abstract In this paper, a new image reconstruction algorithm employing dynamic grids technique is proposed for tomographic gamma scanning. The key feature of the algorithm is the use of adaptive grid refinement in areas that indicate large values. Simulation results show that the application of dynamic grids has a good performance in emission reconstruction with a distinct advantage in the accurate positioning of the 'hot spots' and reducing the number of grids, but doesn't achieve a tangible improvement in transmission reconstruction.

Key words Tomographic gamma scanning, Emission reconstruction, Transmission reconstruction, Dynamic grids

1 Introduction

In order to satisfy the safety demands, the distribution of the radioactivity must be measured before the storage, transportation and final disposition of the conditioned radioactive waste drums. Non-destructive assay (NDA) techniques are widely used for routine quality checking of radioactive waste drums^[1,2], and tomographic gamma scanning (TGS) method is an advanced NDA technique which can obtain the radionuclide distributions.

The TGS method performs tomographic transmission and emission scans on the waste drum. The transmission scan aims at the image of matrix density which is used to make point-to-point attenuation corrections for the emission image of activity distribution^[3-5]. The first TGS system was established by Los Alamos National Laboratory (LANL) in early 1990s^[5]. So far, there are already commercial grade TGS systems for nuclear power plant applications^[6,7].

In the existing TGS technique, the image is presented by a simple voxel model which consists of a series of fixed uniform cells^[5-10]. It is assumed that the density and the radioactive concentration are uniform

within a voxel. However, it is supposed that more emphasis should be placed on the voxels with large density and radioactivity mainly because of two reasons: first, the high density matrix will cause serious gamma ray attenuation; second, the accuracy of the total activity depends to a large extent on the accuracy of the 'hot spot' activity.

In this paper, dynamic grids technique is applied in TGS image reconstruction which can automatically adapt to the reconstructed distribution by refining the grids in areas with large values. In order to simplify the calculation, the 2-D situation of one segment in the waste drum is investigated.

2 Method

2.1 Transmission Measurement of TGS

According to Beer's law, the transmission measurement is described by

$$CT_i = C_0 \cdot \exp\left(-\sum l_{ij} \cdot u_j\right) \quad (1)$$

where, C_0 is the count rate of the transmission source without attenuation; CT_i is the photon count rate in the i 'th transmission measurement attenuated by the waste drum; l_{ij} is the track length of the j 'th voxel along a ray connecting the transmission source and the detector

crystal in the i 'th measurement; u_j is the linear attenuation coefficient of the j 'th voxel.

Eq.(1) can be converted into Eq.(2) as follows

$$v_i = \sum l_{ij} \cdot u_j \quad (2)$$

where,

$$v_i = -\ln(CT_i / C_0) \quad (3)$$

Then, the transmission image can be obtained by solving the linear system

$$v = L \cdot \mu \quad (4)$$

where,

$$v = (v_1, v_2, v_3, \dots, v_I)^T$$

$$\mu = (\mu_1, \mu_2, \mu_3, \dots, \mu_J)^T$$

I is the number of measurements and J is the number of voxels.

L is a $I \times J$ thickness matrix consisting of each element l_{ij} as described in Eq.(1).

2.2 Emission Measurement of TGS

The emission problem is described by the linear system

$$CE_i = \sum_{0 < j \leq J} \alpha \varepsilon_{ij} a_{ij} A_j \quad (5)$$

where, α is the branching ratio of interested gamma line, CE_i is the count rate of the emission source in the i 'th emission measurement; A_j is the activity of the emission source in the j 'th voxel; ε_{ij} is the detection efficiency which is the probability that a photon emitted from the j 'th voxel will be detected in the i 'th measurement without attenuation; a_{ij} is the attenuation correction factor as described in Eq.(6)

$$a_{ij} = \prod_{k \leq J} \exp(-l_{ijk} \cdot \mu_k) \quad (6)$$

where, l_{ijk} is the linear thickness of the k 'th absorbing voxel along a ray connecting the j 'th emitting voxel and the detector in the i 'th measurement.

Then, the emission image can be obtained by solving the linear system

$$CE = \alpha F \cdot A \quad (7)$$

where,

$$CE = (CE_1, CE_2, CE_3, \dots, CE_I)^T,$$

$$A = (A_1, A_2, A_3, \dots, A_J)^T$$

$$F = \begin{bmatrix} \varepsilon_{11} a_{11} & \cdots & \varepsilon_{1j} a_{1j} & \cdots & \varepsilon_{1J} a_{1J} \\ \vdots & & \vdots & & \vdots \\ \varepsilon_{i1} a_{i1} & \cdots & \varepsilon_{ij} a_{ij} & \cdots & \varepsilon_{iJ} a_{iJ} \\ \vdots & & \vdots & & \vdots \\ \varepsilon_{I1} a_{I1} & \cdots & \varepsilon_{Ij} a_{Ij} & \cdots & \varepsilon_{IJ} a_{IJ} \end{bmatrix}$$

where, F is the attenuation-correction efficiency matrix.

2.3 Adaptive Grid Refinement

A grid refinement strategy is developed in order to automatically adapt to the reconstructed distribution by refining the grids in areas with large values.

Firstly, the grids are sorted by the initial reconstructed values from large to small, then some grids with large values will be refined if the following four conditions are all satisfied:

(1) $x_j \geq \xi \cdot \bar{x}$. The value of the grid x_j is larger than a threshold. Here, the threshold is set to be $\xi \cdot \bar{x}$, and \bar{x} is the average value of the image, ξ is a parameter to control the threshold.

(2) $N_{\text{step}} \leq N_{\text{max,step}}$. The number of grids selected for refinement in each step N_{step} cannot exceed $N_{\text{max,step}}$ ensuring that a certain number of grids are left for refinement in the next step.

(3) $N_{\text{total}} \leq N_{\text{max}}$. The total number of grids N_{total} is less than the maximum value which will be determined by the number of measurements.

(4) Not the smallest size. The base grids with the smallest size are defined as shown in Fig.1(a), dividing the segment into 8 parts in radial direction and 48 angles in circumferential direction. If a grid is already the smallest size, it will not be refined. Fig.1b shows the refinement of a fan-shaped grid. And Fig.1c shows the refinement of a polar grid.

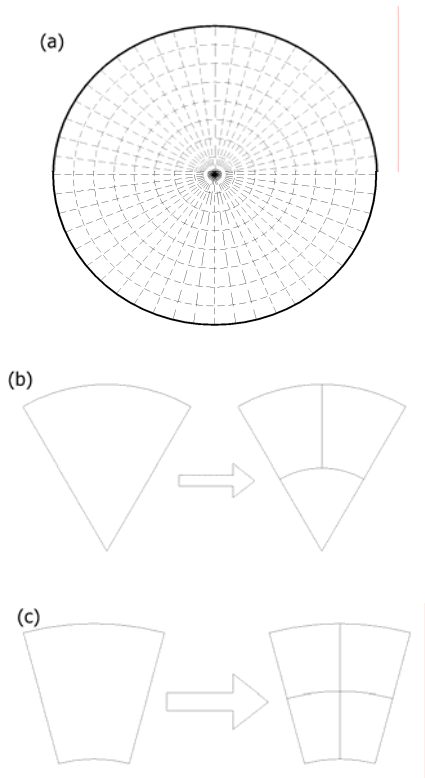


Fig.1 Sketch of grids refinement. The smallest grids(a), the refinement of a fan-shaped grid (b) and the refinement of a polar grid (c).

3 Simulation model

The simulation model is given in Fig.2. The drum is a $\Phi 56$ cm cylinder of 1.2-mm wall thickness. A well type HPGe crystal of $\Phi 6.2$ cm \times 5.95 cm, wrapped by an aluminum layer of 1.5 mm thickness, is housed by a cylindrical lead shield of 4-cm thickness, and positioned at 53-cm away from the drum center. The collimator hole is of 6 cm \times 6 cm \times 15 cm.

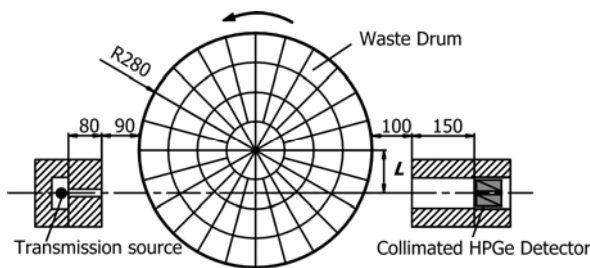


Fig.2 Sketch of simulation model.

The detector is positioned at four horizontal positions ($L=3.5, 10.5, 17.5$ and 24.5 cm), and the drum is rotated step by step with every 15° . So, 96 discrete measurements are taken for one segment.

The measurement sample is given in Fig.3. The heterogeneous matrix shown in Fig.3a consists of two densities, the density of light color area is $1.0 \text{ g}\cdot\text{cm}^{-3}$ and the dark color area is $2.5 \text{ g}\cdot\text{cm}^{-3}$. ^{152}Eu is chosen as the transmission source. As seen in Fig.3b, the ^{137}Cs (661.7 keV) point source is placed at 12 different positions with 5 different radius inside the drum. All the transmission and emission measurements are simulated by MC method.

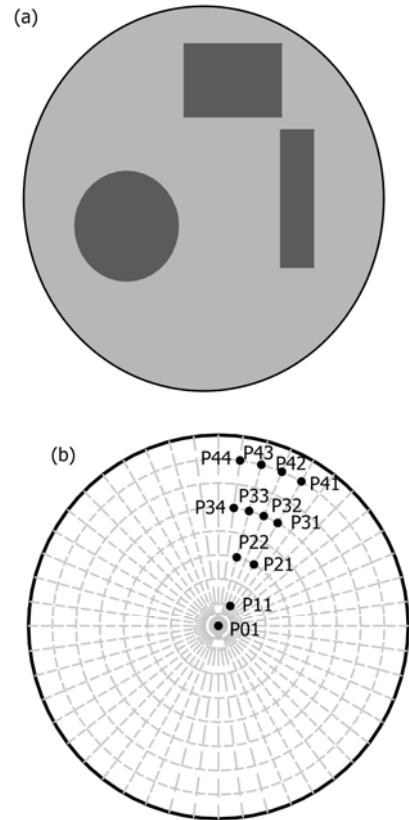


Fig.3 Layout of the measurement sample in the waste drum, the density distribution (a) and the positions of point source (b).

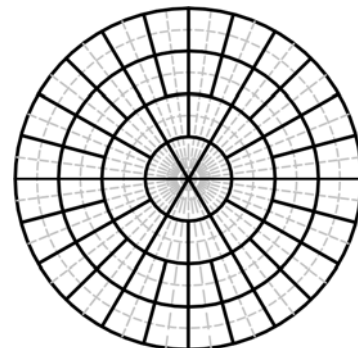


Fig.4 Sketch of the fixed grids for transmission reconstruction.

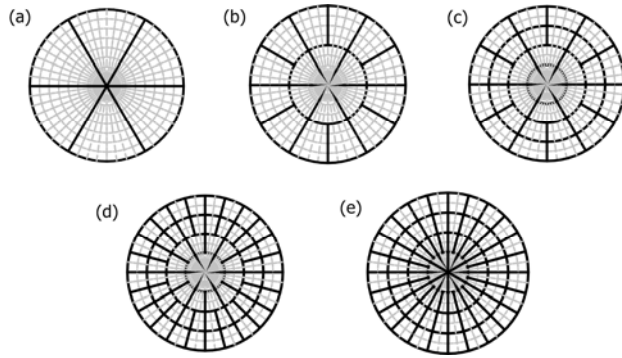


Fig.5 Sketch of five types of fixed grids for emission reconstruction. (a) 6 grids, (b) 18 grids, (c) 36 grids, (d) 66 grids and (e) 84 grids.

Fixed grids and dynamic grids are both used in image reconstruction for comparison. The fixed grids in transmission reconstruction are shown in Fig.4, containing a total of 66 grids. Five types of fixed grids in emission reconstruction shown in Fig.5, which contains 6, 18, 36, 66, 84 grids respectively, are investigated in order to compare the activity reconstruction results of different grids. The grids in Fig.5a is selected to be the initial grids of dynamic grids for both transmission and emission reconstruction. The grid refinement strategy is previously described in section 2.3, and the values of the parameters for the 2-D situation in this paper are as follows: $\zeta=0.25$, $N_{\max, \text{step}}=18$, $N_{\max}=96$.

4 Results and discussion

In this paper, the linear systems Eq.(4) and Eq.(7) are solved by Maximum Likelihood-Expectation Maximization (ML-EM) algorithm^[11]. In order to compare the reconstruction image and the true image, the relative error of the transmission reconstruction image is defined as Eq.(8). The relative error of the emission reconstruction image is defined as Eq.(9)

$$\Delta T = \frac{1}{\bar{\rho}_{\text{true}}} \sqrt{\sum \frac{s_j}{s} \cdot (\rho_j - \rho_{j, \text{true}})^2} \quad (8)$$

$$\Delta E = \frac{\sum A_j - A_{\text{true}}}{A_{\text{true}}} \times 100\% \quad (9)$$

where, ρ_j and A_j are the reconstructed values of the j 'th grid in transmission and emission reconstruction image respectively; $\rho_{j, \text{true}}$ is the true density of the j 'th grid; $\bar{\rho}_{\text{true}}$ is the average density of the segment; s_j is the area of the j 'th grid, s is the area of the segment; A_{true} is the total true activity.

4.1 Transmission reconstruction

The result of transmission reconstruction using fixed grids is shown in Fig.6. It exhibits that the locations of the three high-density regions are approximately in agreement with the measurement sample. The relative error is 0.37.

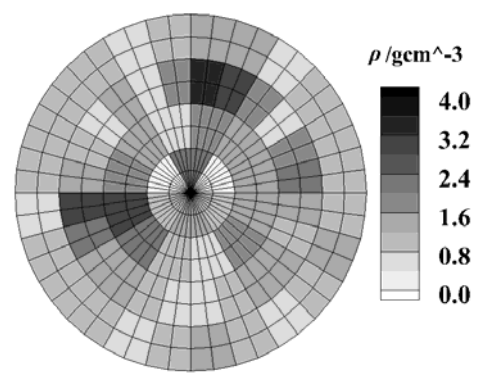


Fig.6 Transmission reconstruction result with fixed grids.

Figure 7 shows the result of transmission reconstruction using dynamic grids. Fig.7(a) is the layout of the final grids, which contains a total of 96 grids. It can be seen that the grids in high-density regions are refined. However, the relative error of the density distribution map as shown in Fig.7b is 0.41, larger than that of fixed grids.

The reason why the transmission reconstruction image using dynamic grids does not get better may be that, the track lengths of transmission rays passing through the refined grids in high-density regions are short (or even zero), so that the coefficients concerned the grids in linear system Eqs.(4) are also small, probably leading to a larger error in solving the equations.

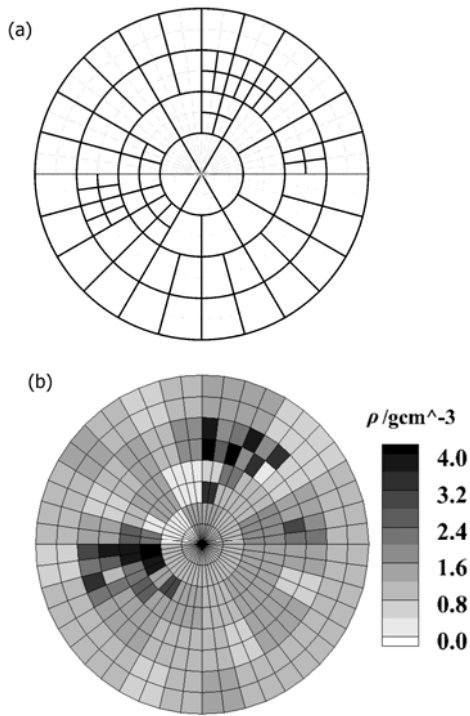


Fig.7 Transmission reconstruction result using dynamic grids. (a) Layout of final grids and (b) Layout of density.

4.2 Emission reconstruction

Since the transmission reconstruction result using dynamic grids is not good as that of fixed grids, the emission reconstruction will be implemented based on the density distribution obtained by using fixed grids.

Fig.8 is the process of grids refinement in emission reconstruction using dynamic grids for point source P41. It can be seen that the grids with large values are refined step by step from Fig.8a to Fig.8d. Small grids are located around the point source in the final step. Generally, the refinement of grids can be finished in 4 or 5 steps for the 2-D situation in this paper.

The final layouts of refined grids in emission reconstruction for several point source cases are listed in Figs.9a, 9b, 9c corresponding with the single point source P11,P21,P31 respectively, and 9d is the grids layout for the multiple source case superposition of all the twelve point sources.

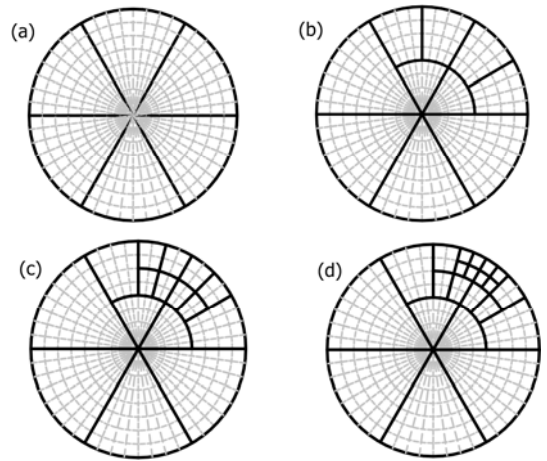


Fig.8 Grids refinement in emission reconstruction for P41. (a) Step 1, (b) Step 2, (c) Step 3 and (d) Step 4.

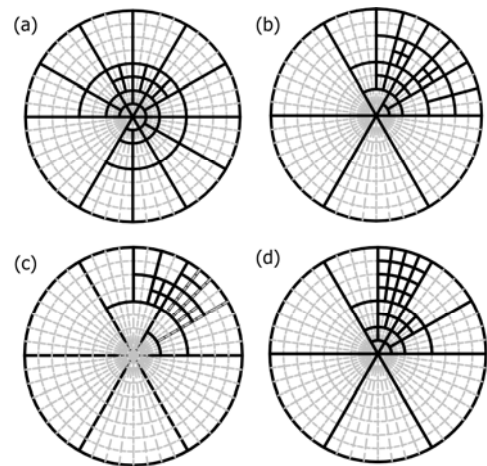


Fig.9 Final layout of refined grids for P11, P21, P31 and all points, (a) P11, (b) P21, (c) P31 and (d) All.

The comparison of the emission reconstruction results using fixed grids and dynamic grids is shown in Fig.10. The abscissa represents the number of grids and the vertical ordinate represents the relative error of the total reconstruction activity. For the symbol of the curve, the first three characters represent the location of the point sources, and the last character represents the kind of grids used in reconstruction where F means fixed grids and D means dynamic grids. The reconstruction results using five types of fixed grids and the results of each step in dynamic grids reconstruction are both shown in the figures.

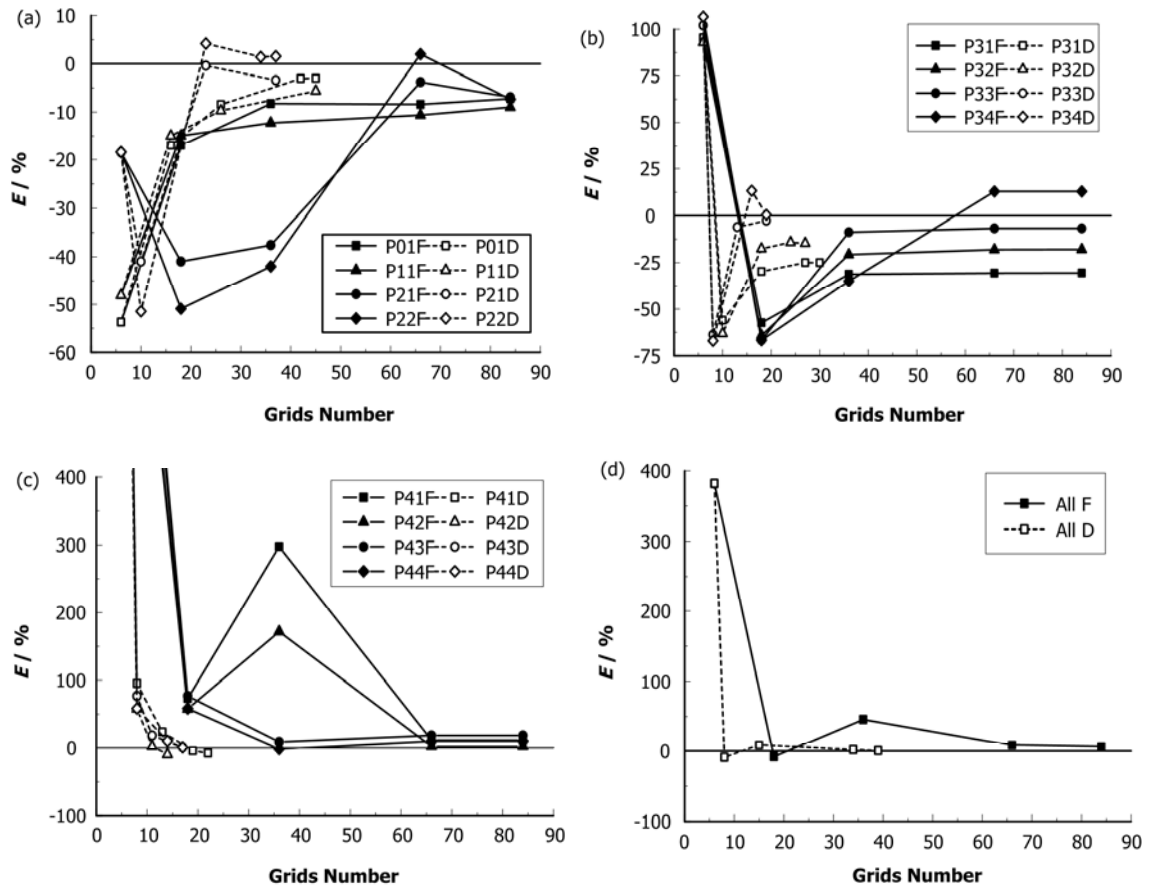


Fig.10 Comparison of emission reconstruction results using fixed and dynamic grids. (a) P0,P1,P2, (b) P3, (c) P4, and (d) All points.

It can be seen from Fig.10 that when the number of grids is small, the errors of the emission reconstruction results are relatively large. With the increase of the grids number, the errors of the emission reconstruction results gradually decrease. The reason is that when the grids become smaller, there will be a grid whose center is very close to the point source, so that the coefficient of this grid in the linear equation system will be more accurate. However, there are accidental cases. For example, the reconstruction error of using 6 fixed grids is smaller than that of using 18 fixed grids for the point source P21 and P22 in Fig.10a. When the center of a grid is just very close to the point source despite the coarse grids, the reconstruction result is also relatively good in this case.

Generally, the reconstruction errors of point sources near the drum wall, such as P41, P42, P43, P44, are relatively large compared with the point sources near the drum center. This is due to the fact that when the point source is close to the drum wall, it

will be close to the detector after rotating a certain angle, and the distance between the source and the detector will greatly impacts on the detection efficiency. As a result, the positional deviation between the grid center and the point source will result in a large deviation in detection efficiency as well as the reconstruction value.

For the cases of a single point source, the reconstruction results of dynamic grids are mostly satisfactory, and the number of the final dynamic grids is much less than that of fixed grids. When the number of grids is the same, the reconstruction results of dynamic grids are better than those of fixed grids, especially for the point source near the drum wall. That's due to the fact that when the grids in the vicinity of the point source are refined, the center of the grid where the point source is located will be closer to the point source, which lead to the accuracy improvement of the attenuation-corrected detection efficiency. However, the detection efficiency in the drum center

area is less sensitive to the source position than that in the area near the drum wall, so the improvement caused by dynamic grids for the point sources near the drum center is not so obvious. For the case of multiple point sources as shown in Fig.10d, the number of the final dynamic grids is also much less than that of fixed grid and the reconstruction result is better. It can be indicated that using dynamic grids in emission reconstruction has a distinct advantage in the accurate positioning of the 'hot spots' and reducing the number of grids.

The errors of the emission reconstruction results for all the 13 cases are listed in Table 1. Here, the fixed grids are previously shown in Fig.4e, containing 84 grids. It can be seen that the number of final dynamic grids is from 14 to 45, much less than 84, roughly two to six times smaller than the number of fixed grids. The results of using dynamic grids are better than those of using fixed grids in 12 cases. It should be mentioned that the error of the multiple source case is relatively acceptable, which is caused by the superposition of the positive or negative error of the single point sources at different positions.

Table 1 Results of emission reconstruction

No.	Point	Fixed Grids		Dynamic Grids	
		Number of Grids	$\Delta E / \%$	Number of Grids	$\Delta E / \%$
1	P01	84	-7.20	45	-3.00
2	P11	84	-8.98	45	-5.62
3	P21	84	-6.91	37	-3.39
4	P22	84	-7.33	37	1.56
5	P31	84	-30.62	30	-25.04
6	P32	84	-17.99	27	-14.65
7	P33	84	-6.78	19	-2.66
8	P34	84	12.81	19	0.47
9	P41	84	11.62	22	-7.78
10	P42	84	2.42	14	-9.55
11	P43	84	18.45	17	0.89
12	P44	84	10.18	17	1.04
13	All	84	6.56	39	0.76

According to the above analysis, using dynamic grids in emission reconstruction can give a more accurate result and reduce the number of grids compared with the fixed grids in most cases.

5 Conclusion

In this paper, a novel image reconstruction algorithm using dynamic grids for TGS reconstruction is demonstrated. The key feature of the algorithm is the use of adaptive grid refinement in areas that indicate large values. The simulation results demonstrate that dynamic grids in emission reconstruction outperform the fixed grids in terms of the accuracy and 'hot spots' positioning in most cases. Furthermore, it can reduce the number of unknowns, which has a clear benefit in the computation time. But using dynamic grids in transmission reconstruction doesn't achieve a tangible improvement. More simulation and experiments on an automatic TGS system will be carried out in the further work to validate the algorithm in 3-D situation.

References

- 1 Reily D, Ensslin N, Smith H, *et al.* Passive Nondestructive Assay of Nuclear Materials, Los Alamos National Laboratory, 1991, 218–234.
- 2 Becker G, McIlwain M and Connolly M. Transuranic and Low-Level Boxed Waste Form Nondestructive Assay Technology Overview and Assessment, Idaho National Engineering and Environmental Laboratory, 1999, 76–89.
- 3 Estep R J. Trans Am Nucl Soc, 1990, **62**: 178–178.
- 4 Kawasaki S, Kondo M, Lzumi S, *et al.* Appl Radiat Isot, 1990, **41**: 983–987.
- 5 Estep R J, Prettyman T H, Sheppard G A. Nucl Sci Eng, 1994, **118**: 145–152.
- 6 Venkataraman R, Croft S, Villani M, *et al.* The next generation tomographic gamma scanner, Annual Symposium on Safeguards and Nuclear Material Management, London, UK, May 10-12, 2005.
- 7 Venkataraman R, Villani M, Croft S, *et al.* Nucl Instrum Meth Phys Res A, 2007, **579**: 375–379.
- 8 Wang T F, Martz H E, Roberson G P, *et al.* Nucl Instrum Meth Phys Res A, 1994, **353**: 672–67.
- 9 Camp D C, Martz H E, Roberson G P, *et al.* Nucl Instrum Meth Phys Res A, 2002, **495**: 69–83.
- 10 Zhang Q H, HUI W H, WANG D, *et al.* Nucl Sci Tech, 2010, **21**: 177–181.
- 11 Shepp L A, Vardi Y. IEEE Trans Med Imag, 1982, **MI-1**: 113–122.